IOP Publishing Phys. Med. Biol. 66 (2021) 175001 https://doi.org/10.1088/1361-6560/ac1b37

Physics in Medicine & Biology

IPEM Institute of Physics and Engineering in Medicine

RECEIVED
27 April 2021

REVISED
3 August 2021

ACCEPTED FOR PUBLICATION
6 August 2021

PUBLISHED
23 August 2021

PAPER

Reverberant shear wave phase gradients for elastography

J Ormachea and K J Parker

Department of Electrical and Computer Engineering, University of Rochester, 724 Computer Studies Building, PO Box 270231, Rochester, NY 14627, United States of America

E-mail: kevin.parker@rochester.edu

Keywords: elastography, ultrasound, MRI, OCT, bio-imaging, viscoelasticity, medical imaging

Abstract

Reverberant shear wave fields are produced when multiple sources and multiple reflections establish a complex three-dimensional wave field within an organ. The expected values are assumed to be isotropic across all directions and the autocorrelation functions for velocity are expressed in terms of spherical Bessel functions. These results provide the basis for adroit implementations of elastography from imaging systems that can map out the internal velocity or displacement of tissues during reverberant field excitations. By examining the phase distribution of the reverberant field, additional estimators can be derived. In particular, we demonstrate that the reverberant *phase gradient* is shown to be proportional to the local value of wavenumber. This phase estimator is less sensitive to imperfections in the reverberant field distribution and requires a smaller support window, relative to earlier estimators based on autocorrelation. Applications are shown in simulations, phantoms, and *in vivo* liver.

1. Introduction

The field of elastography has progressed vigorously over the last 30 years in terms of techniques and clinical applications (Ormachea and Parker 2020b). Within the wide range of techniques available for imaging the elastic properties of soft tissues are several different approaches that can be classified by the type of excitation applied. Major categories in elastography include transient excitation, slow compression, and sinusoidal steady state 'harmonic' shear wave propagation applied to tissues and organs (Doyley 2012). Within the broad class of harmonic shear wave techniques lie several strategies, including most magnetic resonance elastography techniques (Muthupillai *et al* 1995, Plewes *et al* 1995, Sinkus *et al* 2000, Weaver *et al* 2001). For example, the multi-frequency dual elastovisco inversion technique derives the shear modulus and a viscous component, by a least squares error solution based on the Helmholtz equation (Hirsch *et al* 2014, Hetzer *et al* 2019). Furthermore, in ultrasound inversion techniques, vibro-elastography is a multi-frequency shear wave strategy whereby an external source is applied to the tissue and a model is fit to the resulting steady state tissue motion (Turgay *et al* 2006, Eskandari *et al* 2008, Abeysekera *et al* 2015, Honarvar *et al* 2015). In addition, other harmonic shear wave approaches have unique features. For example, Wu *et al* (2004) proposed interference patterns, termed crawling waves, generated from two opposing vibration sources. Chen *et al* (2009) employed a 'push' transducer that transmits a modulated ultrasound beam to produce harmonic vibrations within tissue. The resulting shear waves were monitored using another ultrasound beam. Tzschatzsch *et al* (2016) devised 2D time-harmonic elastography using external harmonic stimulation at multiple frequencies to estimate shear wave speed (SWS) maps. More recently, reverberant shear waves (RSW) (Parker *et al* 2017, Ormachea *et al* 2018, 2019b, Ormachea and Zvietcovich 2021) have been formulated as a distinct approach to elastography. In a reverberant field, a profusion of shear waves along different directions is generated, aided by all the reflections that naturally occur from boundaries and inhomogeneities. Ultrasound imaging techniques can be used to estimate the shear wave amplitude and phase across the region of interest (ROI). Then, the mathematics of a fully three-dimensional (3D) distribution of shear waves enables simple autocorrelation estimators of SWS as a surrogate for stiffness. However, these estimators require an autocorrelation window which can limit the spatial resolution of the SWS

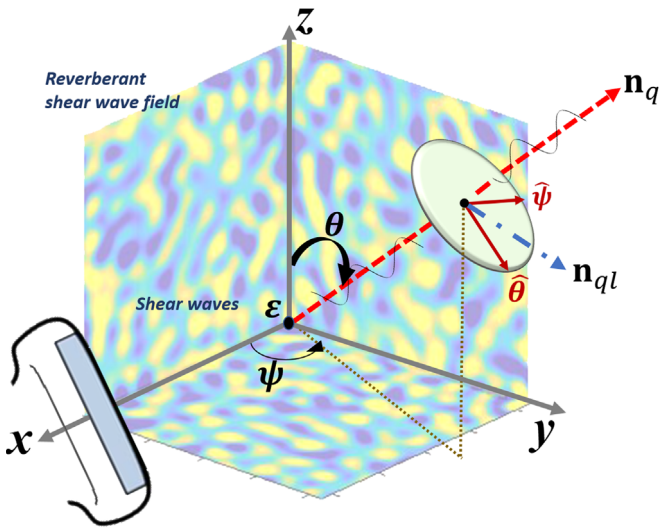

Figure 1. Schematic for the orientation of the imaging transducer (left, which could be ultrasound, magnetic resonance, or optical coherence tomography), and the body that has an isotropic random distribution of shear waves propagating through the interior, consistent with the theory of reverberant fields. The x-axis of the coordinate system is aligned with the axial direction of the imaging transducer, and it is assumed that the imaging system detects motion in the x-direction. The $\mathbf{n}_q$ are the random propagation direction vectors of the q individual plane waves that are distributed throughout the reverberant interior. $\mathbf{n}_{ql}$ are the perpendicular particle velocity vectors parallel to the plane (yellowish disk), formed by basis vectors $\hat{\theta}$ and $\hat{\psi}$, with a particle velocity random amplitude ν_{ql}.

map. Also, there are conditions where the shear wave field may not be reverberant, for example in locations close to a strong source where one wave direction is prominent, and in these situations the descriptive mathematics of reverberant fields may not provide an accurate model. These limitations motivate the search for additional estimators of RSW fields that have high resolution and robust behavior in cases of non-ideal distributions of shear waves.

In this paper, we begin with the establishment of a RSW field, where a set of shear waves in a particular tissue or organ of interest have been established by vibration sources. These vibration sources along with naturally occurring reflections produce multiple shear wave directions propagating within the organ of interest, and multiple frequencies can be established simultaneously. By re-examining the mathematical properties of the RSW field, we derive an improved, efficient, and robust estimator for the tissue viscoelastic properties, specifically the SWS, which can be used to create images of the tissue stiffness and is useful for diagnosing diseases and localizing and classifying lesions. The theory and details of the approach are given in the next sections, then results on phantoms and human livers are presented.

2. Theory

In a fully developed reverberant field depicted in figure 1, the complex pressure and velocity fields at a position ε within the interior can represented as the superposition of plane waves incident from all directions (Pierce 1981, Parker and Maye 1984).

In that case, the vector velocity $\mathbf{v}$ can be written as a function of time t and position ε:

$$\mathbf{v}(t,\,\varepsilon) = \sum_{q,l} \mathbf{n}_{ql} \upsilon_{ql} e^{i(k_0 \mathbf{n}_q \cdot \varepsilon - \omega_0 t)} \tag{1}$$

and where the x component of the velocity is:

$$\upsilon_x(t,\,\varepsilon) = \hat{\mathbf{e}}_x \cdot \mathbf{v}(t,\,\varepsilon) = \sum_{q,l} n_{ql_x} \upsilon_{ql} e^{i(k_0 \mathbf{n}_q \cdot \varepsilon - \omega_0 t)}, \tag{2}$$

$$n_{ql_x} = \mathbf{n}_{ql} \cdot \hat{\mathbf{e}}_x, \tag{3}$$

where the index q represents direction, $\mathbf{n}_q$ are unit vectors uniformly distributed around 4π solid angle, $\mathbf{n}_{ql}$ are the perpendicular particle velocity vectors in the 2π angle within the disk formed by basis vectors $\hat{\theta}$ and $\hat{\psi}$, ν_{ql} is an independent, identically distributed random variable describing the magnitude of particle velocity within a realization of q, and k_0 and ω_0 are the wavenumber and radial frequency of the plane waves, respectively. Taking a snapshot at some fixed reference time t_0, and recognizing that $n_{ql_x} \nu_{ql}$ are independent of position, we examine an ersatz representation of the field:

$$v_x(\varepsilon) = V_0 \mathbf{e}^{i\phi(\varepsilon)}, \tag{4}$$

where V_0 is related to the root mean square amplitude of the field and $\phi(\varepsilon)$ is the spatially varying phase. From Parseval's theorem and the derivative properties of Fourier transforms, following Papoulis (1987) we may equate the second moment of the power spectrum to the derivative of phase. These steps are as follows. Let $P(k)$ be the one-dimensional spatial Fourier transform of $v_x(\varepsilon)$ and where k is the spatial frequency. The power spectrum $|P(k)|^2$ of this function is already known from the ensemble-averaged autocorrelation function $\langle v_x(\varepsilon) v_x(\varepsilon + \boldsymbol{\Delta}\varepsilon)\rangle$ derived previously (Parker *et al* 2017, Zvietcovich *et al* 2019, Aleman-Castañeda *et al* 2021), which can be expressed in terms of spherical Bessel functions. This function depends on the angle θ_s between the imaging system's axis (the direction of detection of motion, the x-axis in figure 1) and the direction of $\boldsymbol{\Delta}\varepsilon$ chosen for the autocorrelation function. For an isotropic medium the autocorrelation function B_{iso} is:

$$B_{\text{iso}}(\Delta\varepsilon, \Delta t) = \overline{V_0^2} e^{i\omega_0 \Delta t} \left\{ \frac{\sin^2\theta_s}{2} \left[j_0(k_0\Delta\varepsilon) - \frac{j_1(k_0\Delta\varepsilon)}{k_0\Delta\varepsilon} \right] + \cos^2\theta_s \frac{j_1(k_0\Delta\varepsilon)}{k_0\Delta\varepsilon} \right\}, \tag{5}$$

where $j_1(\cdot)$ represents the spherical Bessel functions of order 1, and θ_s is the angle between $\boldsymbol{\Delta}\varepsilon$ and $\hat{\boldsymbol{e}}_x$.

Next we examine the derivative of one realization of the field and the corresponding Fourier transform of that function. Denoting:

$$\mathcal{J}\{v_x(\varepsilon)\} = V_0 P(k), \tag{6}$$

$$\mathcal{J}\left\{ \frac{d}{d\varepsilon} v_x(\varepsilon) \right\} = ikV_0 P(k). \tag{7}$$

Now, by taking the magnitude square and equating the two domains using Parseval's theorem, we have, with substitution from equation (4):

$$\begin{aligned} \int \left| \frac{d}{d\varepsilon} v_x(\varepsilon) \right|^2 d\varepsilon &= \frac{V_0^2}{2\pi} \int |(ik)P(k)|^2 dk \\ \int \left| iV_0 \left(\frac{d}{d\varepsilon}\phi(\varepsilon) \right) e^{i\phi(\varepsilon)} \right|^2 d\varepsilon &= \frac{V_0^2}{2\pi} \int k^2 |P(k)|^2 dk \\ \int \left| \frac{d}{d\varepsilon}\phi(\varepsilon) \right|^2 d\varepsilon &= \frac{1}{2\pi} \int k^2 |P(k)|^2 dk. \end{aligned} \tag{8}$$

The right side is also recognized as the second moment m_s^2 of the power spectrum of the RSW field, which has been derived previously (Parker *et al* 2017, Zvietcovich *et al* 2019, Aleman-Castañeda *et al* 2021) and is strictly bandlimited to $\pm k_0$. Specifically for the transverse case ($\theta = \pi/2$):

$$|P(k)|^2 = \frac{\sqrt{\frac{\pi}{2}}(k_0^2 + k^2)}{4k_0^3} \text{ for } |k| \leqslant k_0. \tag{9}$$

To determine the second moment, using s for the spatial frequency variable of integration and considering the orthogonal direction to the measurement axis, we find:

$$m_s^2 = \int_{-k_0}^{k_0} (s^2) \frac{\sqrt{\frac{\pi}{2}}(k_0^2 + s^2)}{4k_0^3} ds = \frac{\sqrt{8\pi}}{15} k_0^2 \tag{10}$$

for transverse direction of the displacement with respect to the imaging system's axis. Then, interpreting the left-hand side of equation (8) as an ensemble average:

$$k_0^2 = \boldsymbol{C} \left\langle \left| \frac{d\phi}{d\varepsilon} \right|^2 \right\rangle, \tag{11}$$

where the brackets indicate the average value over some homogeneous region and $\boldsymbol{C}$ is a scale constant which depends on θ_s (the orientation in equation (5)) and can also be set in practice by comparison to an independent measurement in a reference material.

This analysis can also be extended to two-dimensional estimates. It can be shown that the key relationships including Parseval's theorem (and the related Rayleigh integral theorem), the derivative theorem, and the second moment theorem all have direct extensions to two-dimensional Fourier transforms (Bracewell 1995). Thus, using phase unwrapping, we estimate the phase information across a reverberant field in two transverse dimensions approximately as

$$\phi(x, z) \cong k_x x + k_z z + c_0, \tag{12}$$

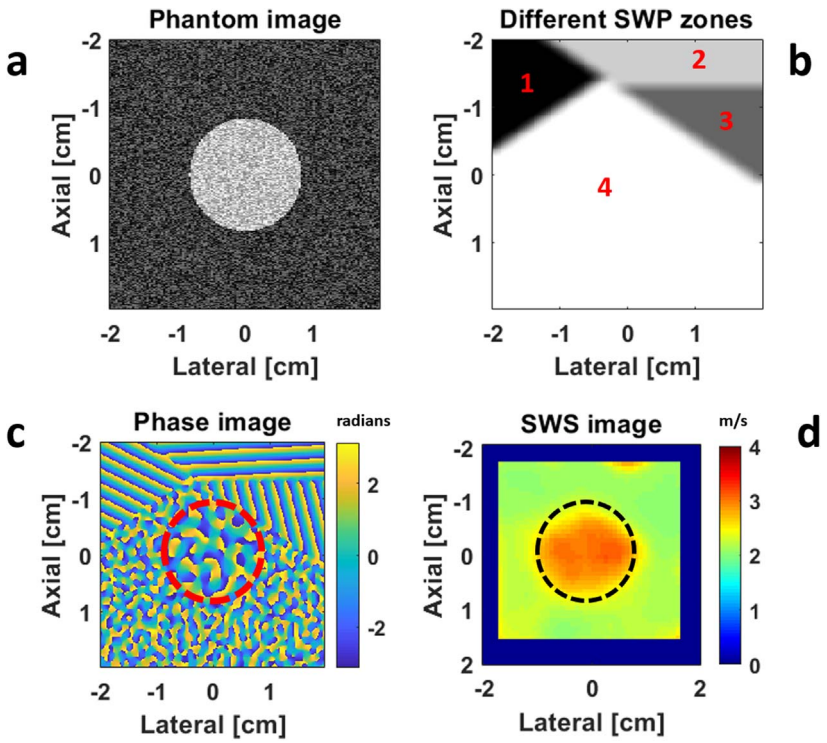

Figure 2. Simulation analysis. (a) Representation of the inclusion and homogeneous media. The SWS for the inclusion and the background are 3.0 and 2.0 m s^{-1}, respectively. (b) Illustration of different regions where shear waves behave as a dominant unidirectional wave (zones 1–3) and as a reverberant shear wave field (zone 4). (c) Phase map of the propagating shear waves, showing that for regions 1–3, planes waves are propagating in different directions. For region 4, a clear reverberation field is observed. The red dashed circle illustrates the inclusion location. (d) Final SWS image applying the phase gradient method. The black dashed circle illustrates the location of the inclusion.

and the wavenumber estimation is formed from the two-dimensional information using

$$k^2 \approx \boldsymbol{C}\left\langle \left| \frac{d\phi}{d\varepsilon} \right|^2 \right\rangle = \boldsymbol{C}(k_x^2 + k_z^2). \tag{13}$$

In a final step, the phase velocity or SWS can be determined by

$$c_s = \frac{2\pi f}{k}, \tag{14}$$

where f is the corresponding vibration frequency, and this sequence can be called the 'phase gradient method'. In other cases where the two axes of an image plane are oriented as transverse and axial with respect to the detection of velocity, then the k_x and k_z will require different scale factors, since the autocorrelation function depends on orientation as given in equation (5). Finally, we note that if the magnitude of $v_x(\varepsilon)$ in equation (4) is taken to be a function of position, the general approach still holds with an additional derivative term in equation (8). The details of this follow the analysis of signal duration and ripple in section 4.4 of Papoulis (1987).

3. Methods

3.1. Materials

3.1.1. Simulations based on a Monte Carlo analysis

Similar to Ormachea *et al* (2019a) and Zvietcovich *et al* (2019), a 40 × 40 × 40 mm^3 field (0.3 mm sampling resolution) was generated in MATLAB (The MathWorks, Inc. Natick, MA, USA) to simulate a RSW field in an linear-elastic medium to validate the SWS estimator. The medium, illustrated in figure 2(a), shows the field containing a harder inclusion (c_s = 3.0 m s^{-1}) surrounded by a softer background (c_s = 2.0 m s^{-1}).

The reverberant field was created with a total of 1000 realizations of random variables: $\mathbf{n}_{ql}$ is defined by the angles of the basis vectors $\hat{\psi}$ and $\hat{\theta}$ (see figure 1), both covering a range of $[0, 2\pi]$ radians; the scalar v_{ql} covers a range of $[-1, 1]$ m s^{-1} representing the particle velocity amplitude. The random realizations generate a spatial and complex valued particle velocity field $V(\varepsilon) = V(\varepsilon)e^{-i\omega t}$, where $\omega_0 = 2\pi f_0$ with f = 900 Hz and $k = c_s/\omega_0$. In addition, a hybrid regional model was made of imperfect reverberant fields comprised of three

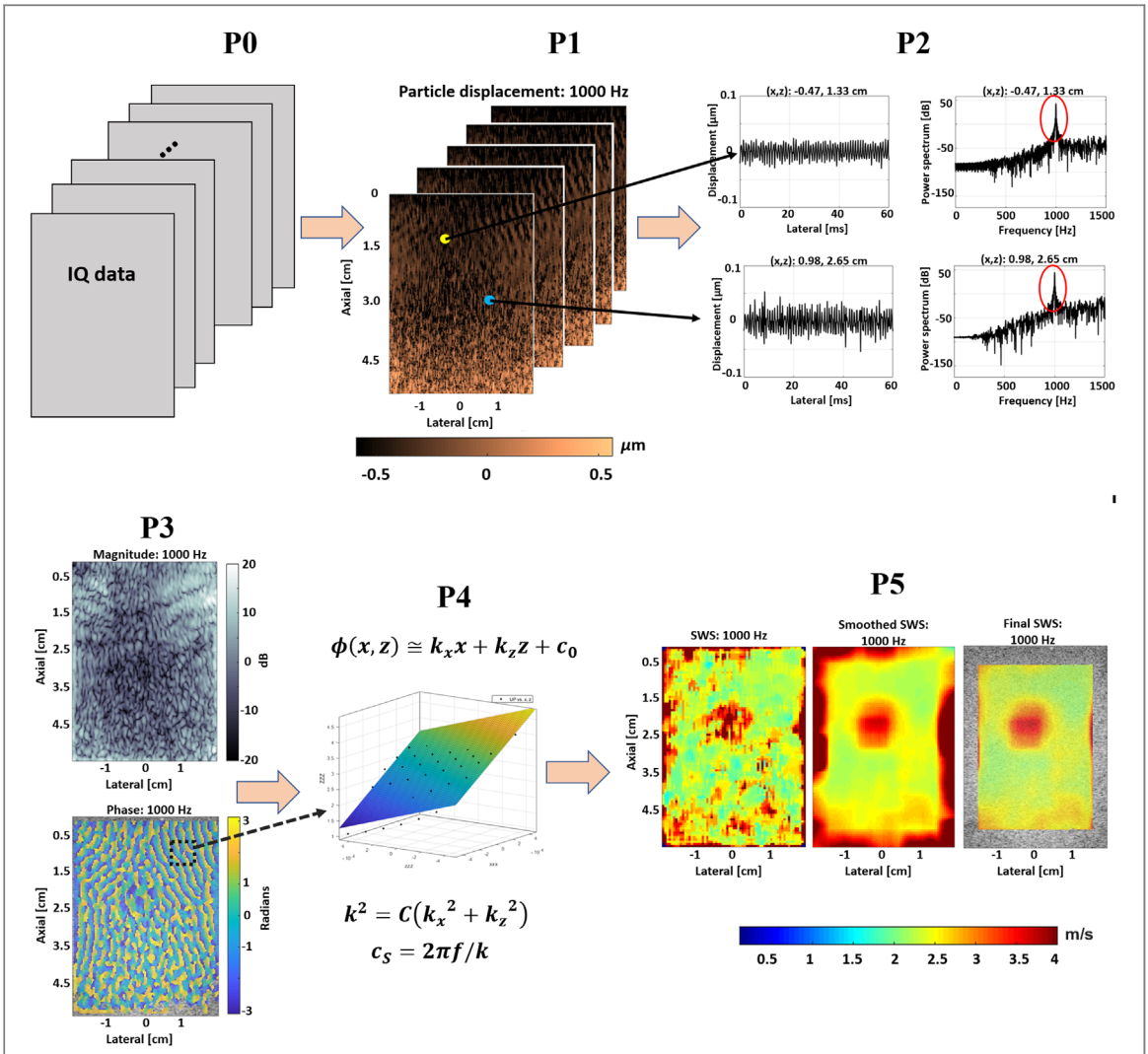

Figure 3. Summary process to obtain the 2D SWS maps for their corresponding vibration frequency. The arrows indicated the process flow starting at procedure (P0) to the final step (P5) displaying the shear wave speed image.

dominant shear waves propagating at different directions through the entire field. Then, four different binary masks with smooth edges were created. Each of them was designed with a particular shape, as can be observed in figure 2(b), and applied. Regions 1–3 were designated for each of the individual plane shear waves simulations and region 4 was selected for the reverberant simulation. After multiplication of each simulation with its corresponding mask, all the results were superimposed to replicate a ROI containing three unidirectional shear waves and one reverberant field. This simulates the presence of various dominant unidirectional shear waves propagating in some regions (areas 1–3 in figure 3(b)) of the field, where there is not a sufficient number of waves over all directions to produce a RSW field or in proximity to a strong external source. Thus, the simulation also evaluates if the phase gradient method could measure the corresponding SWS in a less ideal or 'pre-reverberant' condition.

3.1.2. CIRS phantom and in vivo *liver scans*

Two calibrated phantoms were used in this study. The first was a CIRS breast phantom (Model 059, Computerized Imaging Reference Systems, Norfolk, VA, USA) with background (20 kPa nominal Young's modulus) and inclusion regions (at least two times stiffer than the background region per the manufacturer's datasheet). The other phantom was a custom-made CIRS (Serial No. 2095.1-1, Computerized Imaging Reference Systems) homogeneous viscoelastic phantom (6 kPa nominal Young's modulus). Additionally, one liver tissue from a volunteer was scanned on the custom bed. The scan was conducted under the requirements of informed consent of the University of Rochester Research Subjects Review Board.

3.2. Shear wave elastography methods

3.2.1. RSW phase gradient elastography

Figure 3 summarizes the process to obtain the 2D SWS maps for their corresponding vibration frequency using the phase gradient method in a reverberant shear wave elastography (R-SWE) field. 'P0' estimates the particle displacements, in the axial direction, using a Loupas estimator. 'P1' shows some snapshots of a typical R-SWE field using a 1 kHz vibration frequency. 'P2' illustrates the particle displacement in time and its corresponding frequency spectrum showing the maximum peak at 1 kHz. Then, the signal to noise ratio (SNR) of the particle displacement signals were measured by:

$$\mathrm{SNR} = 10\log_{10}\left(\frac{P_s}{P_n}\right), \tag{15}$$

where P_s and P_n are the average signal power of the particle displacement signal and the power of background noise, respectively. The regions with SNR $<$ 10 dB were neglected and were not used for later steps. After taking the magnitude and phase at the peak, 'P3' applies an additional 2D bandpass spatial filter to remove extremely low frequency compressional waves and reduce high frequency noise in all directions as in (Ormachea *et al* 2018, 2019b). The cutoff spatial frequencies, related to the wavenumber k of the filter were set at $k_{\mathrm{l}} = 2\pi f/c_{\mathrm{h}}$ and $k_{\mathrm{h}} = 2\pi f/c_{\mathrm{l}}$, respectively, where c_{l} and c_{h} are a chosen low and high SWS, respectively. c_{l} was 0.5 m s^{-1} for all experiments, whereas c_{h} was 5 m s^{-1} for the breast phantom and 3 m s^{-1} for the viscoelastic phantom and *in vivo* human liver. 'P4' applies the phase gradient method to obtain the correspondent wavenumber by taking a small ROI (1.34 $\times$ 1.34 mm^2 at 1 kHz, with 1 pixel/0.14 mm) of the unwrapped phase values. The unwrapped phase, obtained using the MATLAB's unwrap function, which we applied to the lateral dimension, is repeated along sequential lines so as to form a plane in 2D which is then fitted to equation (12) using the MATLAB curve-fitting toolkit based on a robust linear least square minimization method. From equation (12), the wavenumber is calculated using equation (13). The 2D wavenumber map is obtained by repeating 'P4' at different pixel locations. Then, the SWS is obtained using equation (14). Finally, 'P5' smooths the 'raw' SWS map by applying a weighted averaging filter mask of 7 $\times$ 7 pixel size as in Jou (2012) and also eliminates the edges.

3.2.2. Shear wave elastography based on acoustic radiation force impulse (ARFI) for comparison purposes

A Samsung ultrasound system (Model RS85, Samsung Medison Co. Ltd, Seoul, South Korea) was used in order to obtain elastography images for comparison purposes for the CIRS phantoms. Displacement waveforms were tracked over time and the phase velocity was obtained by calculating the 2D Fourier transform from the particle velocity signals and finding the maximum amplitude at spatial frequency $k(\omega)$ for each discrete temporal frequency (Nenadic *et al* 2013, Nightingale *et al* 2015). The specific data acquisition and post-processing details to obtain the phase velocity information are described by Ormachea and Parker (2020a). Then, a linear dispersion slope over a specific frequency range was calculated using:

$$c_p(f) = \frac{2\pi f}{k} \tag{16}$$

and

$$c_p(f) = c_0 + \left.\frac{dc}{df}\right|_{f_0} f, \tag{17}$$

where c_0 is the intercept at zero frequency, f is frequency, and $\left.\frac{dc}{df}\right|_{f_0}$ is the linear dispersion slope evaluated at a particular frequency band around f_0. In addition, the power law coefficient was measured from the phase velocity information using

$$c_p(\omega) = c_1(\omega)^a, \tag{18}$$

where c_1 is the phase velocity measured at a reference point, for example at $\omega = 1$ rad s^{-1}, and a is the power law coefficient. The minimum and maximum frequency values for the frequency range correspond to the mean frequency peak and the -6 dB criteria of the spectrum, respectively. The specific data acquisition and post-processing details to obtain the phase velocity information are described by Ormachea and Parker (2020a).

3.3. Experimental setup for RSW phase gradient elastography

3.3.1. Scanner and data acquisition

A Verasonics system (Vantage-128TM, Verasonics, Kirkland, WA, USA) connected to a convex ultrasound probe (model C4-2, ATL, Bothell, WA, USA) or a linear ultrasound probe (model L7-4, ATL, Bothell, WA, USA) was applied. This system was used to track the induced displacements using a Loupas estimator (Loupas *et al* 1995). The linear probe was used for the breast phantom, whereas the convex probe was used for scanning deeper into the viscoelastic phantom and liver tissue. The center frequencies were 2.98 MHz and 5.21 MHz for

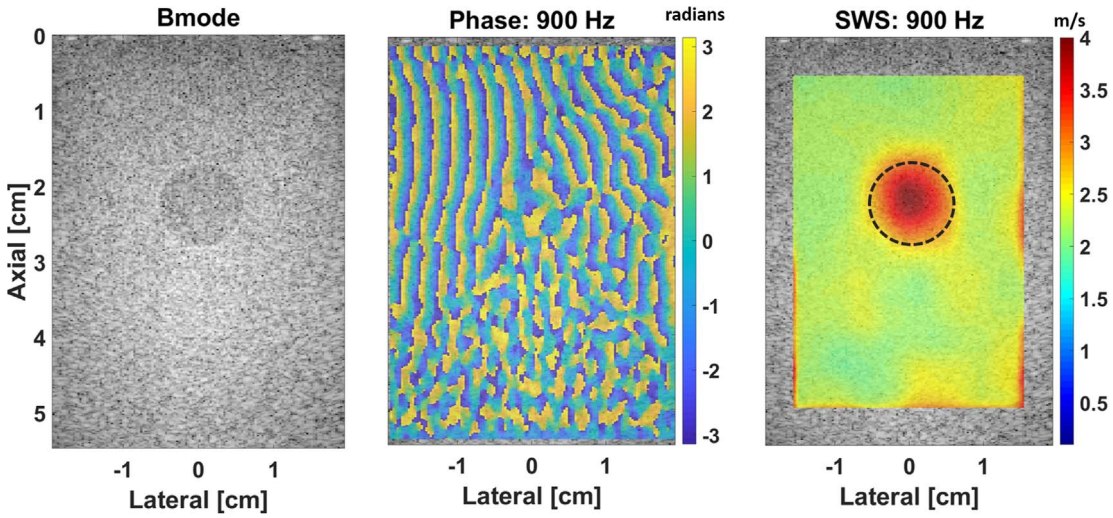

Figure 4. Illustration of shear waves propagating in different direction creating a reverberant field and dominant unidirectional waves in a 'pre-reverberant' field. As illustrated in the simulations, the phase gradient method is able to estimate the SWS for both conditions. (Left) B-mode image of the CIRS breast phantom showing the harder inclusion. (Center) phase map of the propagating shear wave at 900 Hz. (Right) final SWS image showing the harder inclusion and the background. The black dashed circle illustrates the location of the inclusion.

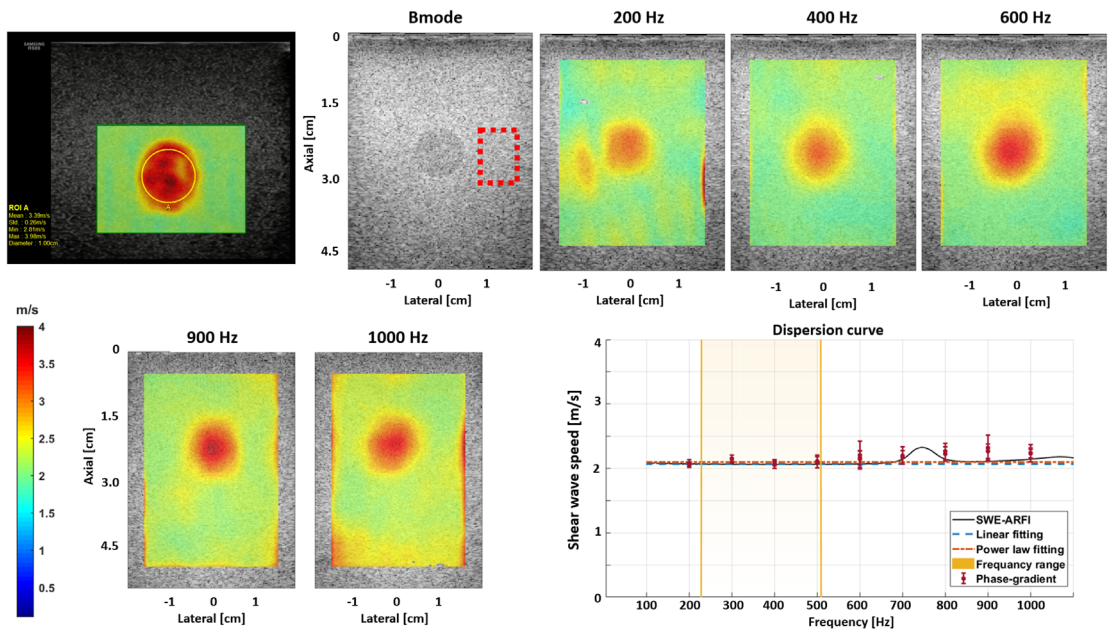

Figure 5. Elastography images corresponding to the CIRS breast phantom showing a stiffer inclusion, its B-mode image, and the dispersion curve. The SWS image obtained with ARFI using the Samsung system is shown on the top left corner. The SWS images obtained with the phase gradient method are shown on the top and bottom rows corresponding to different vibration frequencies: 200 Hz, 400 Hz, 600 Hz, 900 Hz, and 1 kHz. The bottom right corner shows the dispersion curve including phase velocity values (mean $\pm$ standard deviation (SD)) for the Samsung data and the results obtained in this study. The mean and SD were extracted for a ROI in each image. The ROI position is illustrated as a red dashed rectangle in the B-mode image. For this case, phase velocity values almost remain the same for different frequencies, indicating that the material is almost purely elastic. The dispersion curve represents a direct comparison between the Samsung system and the phase gradient method. In addition, the blue dashed line denotes a linear fitting, and the red dashed line denotes a power law fitting. The orange shaded region represents the -6 dB frequency range criteria for the ARFI-based signals. More detail about this criterion can be found in Ormachea and Parker (2020a).

the convex and linear probes, respectively. The sampling frequencies were 12 MHz and 20 MHz for the convex and linear probes, respectively. The frame rate was set to 3600 Hz and 5000 Hz for the convex and linear probes, respectively. A 0° steering angle was used to insonify the medium and the total acquisition time was 0.25 s.

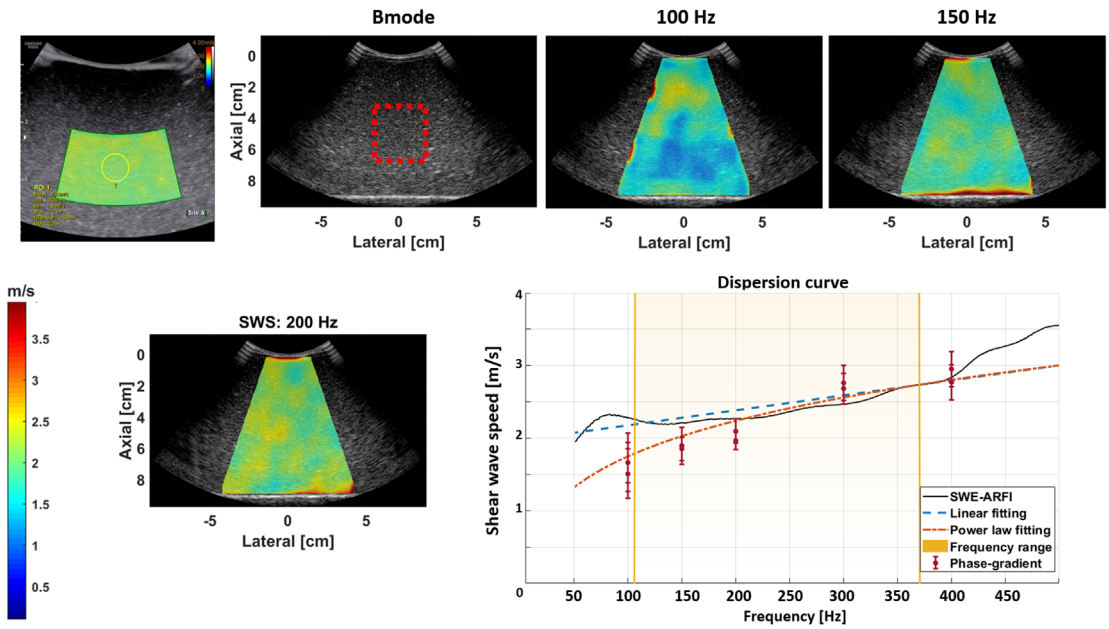

Figure 6. Elastography images corresponding to the CIRS viscoelastic phantom, its B-mode image, and the dispersion curve. The SWS image obtained with ARFI using the Samsung system is shown on the top left corner. The SWS images obtained with the phase gradient method are shown on the top and bottom rows corresponding to different vibration frequencies: 100 Hz, 150 Hz, and 200 Hz. The bottom right corner shows the dispersion curve including phase velocity values (mean ± SD) for the Samsung data and the results obtained in this study. The mean and SD were extracted for a ROI at each image. The ROI position is illustrated as a red dashed rectangle in the B-mode image. For this case, phase velocity values increase as a function of frequency, indicating that the material has viscoelastic properties. The dispersion curve represents a direct comparison between the Samsung system and the phase gradient method. In addition, the blue dashed line denotes a linear fitting, and the red dashed line denotes a power law fitting. The orange shaded region represents the −6 dB frequency range criteria for the ARFI-based signals. More detail about this criterion can be found in Ormachea and Parker (2020a).

3.3.2. Vibration sources and vibration frequency range

A custom-made portable trifold futon (70 × 60 × 10 cm^3) with multiple embedded vibration sources (Quad Resonator Model EI718^{TM}, Elastance Imaging LLC, Columbus, OH, USA) was mounted to a clinical bed to generate the RSW field. The precise details of the active source configuration are proprietary to Elastance Imaging LLC. Vibration frequencies between 100 and 1000 Hz were used for the breast CIRS phantom, whereas frequencies between 100 and 400 Hz were used for the viscoelastic and *in vivo* liver experiments.

4. Results

Figure 2 shows the simulated media illustrating 'pre-reverberant' and RSW fields. Figure 2(c) shows the shear wave phase map and shows the unidirectional propagation in regions 1–3 (figure 2(b)) and the RSW field in region 4 (figure 2(b)). Figure 2(d) shows the final SWS image applying the phase gradient method. The mean and standard deviations for the inclusion and background at 900 Hz are 2.96 ± 0.08 m s^{-1}, and 2.10 ± 0.07 m s^{-1}, respectively, showing good agreement with the SWS values used for the simulation for the inclusion (c_s = 3.0 m s^{-1}) and the background (c_s = 2.0 m s^{-1}).

Figure 4 shows (from left to right) the B-mode, shear wave phase map, and the SWS image for the CIRS breast phantom vibrating at 900 Hz. As illustrated in the simulated case in figure 2, a 'pre-reverberant' zone and more ideal RSW regions can be observed within the entire ROI. The final SWS image using the phase gradient method shows good performance in estimating a consistent SWS for both shear wave fields. The mean SWS and the standard deviations for the inclusion and the background are 3.43 ± 0.24 m s^{-1}, and 2.27 ± 0.19 m s^{-1}, respectively. The CIRS datasheet for this phantom indicates that the background Young's modulus is 20 kPa (~2.58 m s^{-1}) and at least 2 × harder (40 kPa, ~3.65 m s^{-1}) for the inclusions.

Figure 5 shows a comparison of SWS results for the CIRS breast phantom using a commercial system (Samsung RS85, Samsung Medison Co. Ltd, South Korea) and the phase gradient method for different vibration frequencies. Since the commercial elastography image is based on ARFI, the measured SWS is a group velocity value, whereas the phase gradient method measures the phase velocity. For that reason, the dispersion curve, for a background region, was obtained for both methods to perform a direct comparison in terms of phase velocity. As observed, a good agreement between both methods was obtained. For example, the phase velocity at 600 Hz, is 2.14 ± 0.09 and 2.2 ± 0.13 for the Samsung system and the phase gradient method, respectively. The

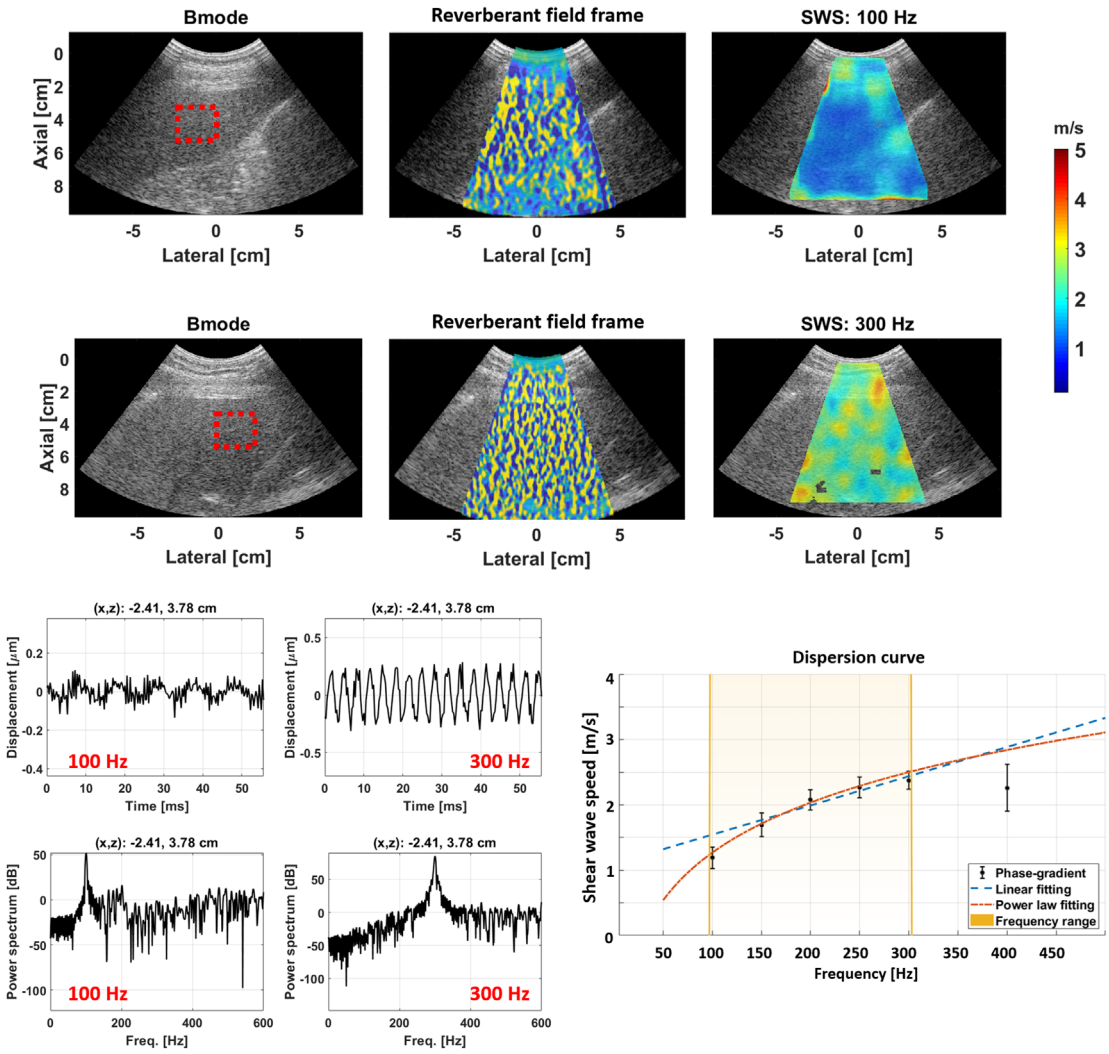

Figure 7. Elastography images corresponding to *in vivo* liver tissue. The SWS images obtained with the phase gradient method are shown in the top rows, corresponding to two vibration frequencies: 100 and 300 Hz. Each of them has its corresponding B-mode image and a snapshot of the reverberant shear wave field to the left. Some regions do not show SWS information because the corresponding particle displacement was neglected due to its low SNR, as explained in section 3.2.1. The bottom left corner shows two particle displacement examples located at specific lateral and axial positions (x, z) with their corresponding spectrum to illustrate that the maximum peak corresponds to the applied vibration frequency. The bottom right corner shows the dispersion curve including phase velocity values (mean $\pm$ SD) for the results obtained in this study. The mean and SD were extracted for a ROI at each image. The ROI's position is illustrated as a red dashed rectangle in the B-mode image. For this case, phase velocity values increase as a function of frequency, indicating that liver tissue has viscoelastic properties. In addition, the blue dashed line denotes a linear fitting, and the red dashed line denotes a power law fitting. The orange shaded region represents the frequency range used to estimate the linear and power law fittings.

estimated linear dispersion slope and the power law coefficient are 0.06 m s^{-1} kHz^{-1} and 0.038, respectively. In this case the dispersion curve remains almost constant since the phantom is an almost purely elastic phantom.

Figure 6 shows a comparison of SWS results for the custom-made CIRS viscoelastic phantom using a commercial system (Samsung RS85) and the phase gradient method for different vibration frequencies. Similar to the CIRS breast phantom case, the dispersion curve was obtained for both methods to perform a direct comparison in terms of phase velocity. As shown, a good agreement between both methods was obtained. For example, the phase velocity at 150 Hz is 2.21 $\pm$ 0.18 and 1.90 $\pm$ 0.25 for the Samsung system and the phase gradient method, respectively. The estimated linear dispersion slope and the power law coefficient are 2.10 m s^{-1} kHz^{-1} and 0.198, respectively. It can also be noticed that the phase velocity increases as a function of frequency since the phantom is a viscoelastic material.

Figure 7 shows SWS images for an *in vivo* liver tissue result applying different vibration frequencies. RSW fields were obtained for the total field of view and complete SWS images were obtained for the liver that is located between 3.5 and 9 cm depth. A dispersion curve was obtained using the mean SWS (phase gradient) values from the ROI. The estimated linear dispersion slope and the power law coefficients are 4.47 m s^{-1} kHz^{-1} and 0.07, respectively.

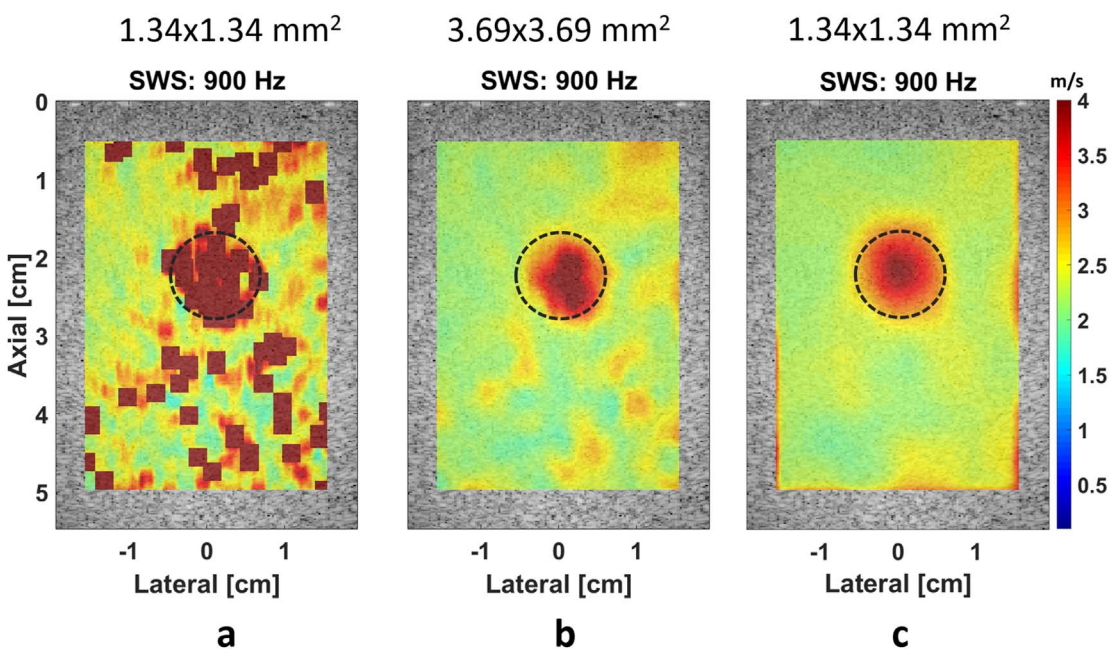

Figure 8. Comparison of SWS images using the approaches based on the autocorrelation (a) and (b) and phase gradient (c) in the CIRS breast phantom at 900 Hz. Both methods require a local window to estimate the wavenumber k (window size is shown above each SWS image). Case (a) is not able to reconstruct the elastography image properly and reports overestimated values of SWS since it does not have enough points, due the small window size, to approximate the theoretical curve. On the other hand, case (b) shows a better result, based on the autocorrelation method, when the window size is increased. Case (c) uses same window size as case (a) and shows an improvement for the SWS. This indicates that the phase estimator is less sensitive to imperfections in the reverberant field distribution and requires a smaller region of support than case (b).

5. Discussion

This approach represents a departure from previous work on RSW fields, which focused on determining the spatial autocorrelation function from which the key parameters k and c could be estimated. In the current method, the raw complex velocity field $v_x(\varepsilon)$ from within the ROI is examined and the key metric is the rate of change of phase. Computationally, both approaches (autocorrelation versus unwrapped phase derivative) require a region of support and an ensemble average in order to provide an estimate of wavenumber k_0. Figure 8 explores and compares, for illustration purposes, the two approaches to estimate the SWS in the CIRS breast phantom. It is observed that the phase gradient is able to measure the SWS using smaller regions than the autocorrelation method. This is important since a smaller window may improve the spatial resolution and its computational cost to process the entire field of view. As illustrated in figure 8, another advantage of the phase method is that it appears to be robust under a variety of wave types. For example, in 'pre-reverberant' fields where there is not a sufficient number of waves over all directions to produce a close match to equation (5), we find that the rate of change of phase still approaches a stable estimate related to k and sensitive to local contrast, as demonstrated in the simulation and phantom experiments represented in figures 2 and 4. Moreover, figure 8 shows that the autocorrelation method estimates have more variation with respect to the orientation of the dominant field direction. It is interesting to note that the ultrasound time-harmonic elastography methods of Tzschatzsch *et al* (2016) make use of a finite difference (spatial derivative) of phase of shear waves in tissue. These are resolved after the application of directional filters, and then the directional phase derivatives are combined as a weighted average according to the relative energy in each directional component. In comparison, the reverberant field approach assumes a fully developed 3D field which is then sampled in any 2D plane or any line within. Directional filters are not required since the assumption is that wave fields from all directions are present and combining in a lawful manner which can be characterized by analytic expressions. A detailed comparison of these different approaches remains for further research.

Finally, we note that a limitation of this work is that the derivations pertain only to a linear-elastic material. Thus, some important rheological complexities of tissue, including viscoelastic loss, and the effects of anisotropy, have not yet been included in this framework. The reverberant field in anisotropic media has recently been analyzed with respect to the key autocorrelation functions along and across the principle axis of anisotropy (Aleman-Castañeda *et al* 2021), presumably the phase gradient would exhibit similar trends but this remains for future research. Attenuation of shear waves introduces a spatially varying term into the equations

and practically speaking, the field will be strongest near the external sources and weakest at the most remote interior region. This requires additional analysis.

6. Conclusion

We have derived a system of determining SWS and dispersion within tissues by carefully examining the spatial progression of phase within a reverberant field. Specifically, the phase derivative obtained from the unwrapped phase is shown to be a robust and accurate measure of k_0, the wavenumber. Since reverberant fields can be created simultaneously at multiple frequencies and separated by transform operations, the wavenumber and phase velocity obtained at multiple frequencies produce dispersion curves that are also useful measures of viscoelasticity. The phase gradient estimators are relatively insensitive to dominant directional waves that can occur in close proximity to external sources and require smaller support regions than do earlier autocorrelation estimators. These results enable rapid, wideband examination of large regions of interest and deep tissue for elastography.

Acknowledgments

The authors thank Christopher Khan for the implementation of the SNR calculation of the particle displacement data. We are also grateful to Elastance Imaging for the loan of their Quad Resonator and for their assistance in data acquisition.

ORCID iDs

J Ormachea https://orcid.org/0000-0003-2481-8133
K J Parker https://orcid.org/0000-0002-6313-6605

References

Abeysekera J, Rohling R and Salcudean S 2015 Vibro-elastography: absolute elasticity from motorized 3D ultrasound measurements of harmonic motion vectors *2015 IEEE Int. Ultrasonics Symp. (IUS)* pp 1–4

Aleman-Castañeda L A, Zvietcovich F and Parker K J 2021 Reverberant elastography for the elastic characterization of anisotropic tissues *IEEE J. Sel. Top. Quantum Electron.* **27** 1–12

Bracewell R N 1995 *Two-Dimensional Imaging* (Englewood Cliffs, NJ: Prentice-Hall) ch 4

Chen S, Urban M W, Pislaru C, Kinnick R, Zheng Y, Yao A and Greenleaf J F 2009 Shearwave dispersion ultrasound vibrometry (SDUV) for measuring tissue elasticity and viscosity *IEEE Trans. Ultrason. Ferroelectr. Freq. Control* **56** 55–62

Doyley M M 2012 Model-based elastography: a survey of approaches to the inverse elasticity problem *Phys. Med. Biol.* **57** R35–73

Eskandari H, Salcudean S E and Rohling R 2008 Viscoelastic parameter estimation based on spectral analysis *IEEE Trans. Ultrason. Ferroelectr. Freq. Control* **55** 1611–25

Hetzer S, Hirsch S, Braun J, Sack I and Weygandt M 2019 Viscoelasticity of striatal brain areas reflects variations in body mass index of lean to overweight male adults *Brain Imaging Behav.* **14** 2477-87

Hirsch S, Guo J, Reiter R, Papazoglou S, Kroencke T, Braun J and Sack I 2014 MR elastography of the liver and the spleen using a piezoelectric driver, single-shot wave-field acquisition, and multifrequency dual parameter reconstruction *Magn. Reson. Med.* **71** 267–77

Honarvar M, Lobo J, Mohareri O, Salcudean S E and Rohling R 2015 Direct vibro-elastography FEM inversion in Cartesian and cylindrical coordinate systems without the local homogeneity assumption *Phys. Med. Biol.* **60** 3847–68

Jou S 2012 Filtering in spatial and frequency domains: examples & tools *Proc. 2012 Int. Conf. on Image Processing, Computer Vision, and Pattern Recognition (IPCV)* vol 1 ed H R Arabnia and L Deligiannidis pp 1087–94

Loupas T, Peterson R B and Gill R W 1995 Experimental evaluation of velocity and power estimation for ultrasound blood flow imaging, by means of a two-dimensional autocorrelation approach *IEEE Trans. Ultrason. Ferroelectr. Freq. Control* **42** 689–99

Muthupillai R, Lomas D J, Rossman P J, Greenleaf J F, Manduca A and Ehman R L 1995 Magnetic-resonance elastography by direct visualization of propagating acoustic strain waves *Science* **269** 1854–7

Nenadic I, Urban M W, Qiang B, Chen S and Greenleaf J 2013 Model-free quantification of shear wave velocity and attenuation in tissues and its *in vivo* application *J. Acoust. Soc. Am.* **134** 4011

Nightingale K R, Rouze N C, Rosenzweig S J, Wang M H, Abdelmalek M F, Guy C D and Palmeri M L 2015 Derivation and analysis of viscoelastic properties in human liver: impact of frequency on fibrosis and steatosis staging *IEEE Trans. Ultrason. Ferroelectr. Freq. Control* **62** 165–75

Ormachea J, Barr R G and Parker K J 2019a 2D shear wave dispersion images using the reverberant shear wave field approach: application in tissues exhibiting power law response *2019 IEEE Int. Ultrasonics Symp. (IUS)* pp 205–8

Ormachea J, Castaneda B and Parker K J 2018 Shear wave speed estimation using reverberant shear wave fields: implementation and feasibility studies *Ultrasound Med. Biol.* **44** 963–77

Ormachea J and Parker K J 2020a Comprehensive viscoelastic characterization of tissues and the inter-relationship of shear wave (group and phase) velocity, attenuation and dispersion *Ultrasound Med. Biol.* **46** 3448–59

Ormachea J and Parker K J 2020b Elastography imaging: the 30 year perspective *Phys. Med. Biol.* **65** 24TR06

Ormachea J, Parker K J and Barr R G 2019b An initial study of complete 2D shear wave dispersion images using a reverberant shear wave field *Phys. Med. Biol.* **64** 145009

Ormachea J and Zvietcovich F 2021 Reverberant sear wve eastography: a multi-modal and multi-scale approach to measure the viscoelasticity oroperties of soft tissues *Front. Phys.* **8** 606793
Papoulis A 1987 *The Fourier Integral and its Applications* (New York: McGraw-Hill) ch 4.4
Parker K J and Maye B A 1984 Partially coherent radiation from reverberant chambers *J. Acoust. Soc. Am.* **76** 309–13
Parker K J, Ormachea J, Zvietcovich F and Castaneda B 2017 Reverberant shear wave fields and estimation of tissue properties *Phys. Med. Biol.* **62** 1046–61
Pierce A D 1981 *Acoustics: an Introduction to its Physical Principles and Applications* (New York: McGraw-Hill)
Plewes D B, Betty I, Urchuk S N and Soutar I 1995 Visualizing tissue compliance with MR imaging *J. Magn. Reson. Imaging* **5** 733–8
Sinkus R, Lorenzen J, Schrader D, Lorenzen M, Dargatz M and Holz D 2000 High-resolution tensor MR elastography for breast tumour detection *Phys. Med. Biol.* **45** 1649–64
Turgay E, Salcudean S and Rohling R 2006 Identifying the mechanical properties of tissue by ultrasound strain imaging *Ultrasound Med. Biol.* **32** 221–35
Tzschatzsch H, Nguyen Trong M, Scheuermann T, Ipek-Ugay S, Fischer T, Schultz M, Braun J and Sack I 2016 Two-dimensional time-harmonic elastography of the human liver and spleen *Ultrasound Med. Biol.* **42** 2562–71
Weaver J B, Van Houten E E, Miga M I, Kennedy F E and Paulsen K D 2001 Magnetic resonance elastography using 3D gradient echo measurements of steady-state motion *Med. Phys.* **28** 1620–8
Wu Z, Taylor L S, Rubens D J and Parker K J 2004 Sonoelastographic imaging of interference patterns for estimation of the shear velocity of homogeneous biomaterials *Phys. Med. Biol.* **49** 911–22
Zvietcovich F, Pongchalee P, Meemon P, Rolland J P and Parker K J 2019 Reverberant 3D optical coherence elastography maps the elasticity of individual corneal layers *Nat. Commun.* **10** 4895